


RESEARCH PAPER

OPEN ACCESS



Zika virus-induced neuro-ocular pathology in immunocompetent mice correlates with anti-ganglioside autoantibodies

Jacob T. Beaver^a, Lisa K. Mills^a, Dominika Swieboda^a, Nadia Lelutiu^a, Edward S. Esser^a, Olivia Q. Antao^a, Eugenia Scountzou^b, Dahnide T. Williams^a, Nikolaos Papaioannou^c, Elizabeth Q. Littauer^a, and Ioanna Skountzou ^a

^aDepartment of Microbiology & Immunology, Emory University School of Medicine, Atlanta, GA, USA; ^bEyeVetSurgery-Small Animal Clinic, Athens, Greece; ^cFaculty of Veterinary Medicine, Aristotle University of Thessaloniki, Thessaloniki, Greece

ABSTRACT

A severe consequence of adult Zika virus (ZIKV) infection is Guillain-Barré Syndrome (GBS), where autoreactive antibodies attack peripheral and central nervous systems (CNS) resulting in neuro-ocular pathology and fatal complications. During virally induced GBS, autoimmune brain demyelination and macular degeneration correlate with low virus neutralization and elevated antibody-mediated infection among Fcγ-R bearing cells. The use of interferon-deficient mice for ZIKV studies limits elucidation of antibody-dependent enhancement (ADE) and long-term pathology (≥120 days), due to high lethality post-infection. Here we used immunocompetent BALB/c mice, which generate robust humoral immune responses, to investigate long-term impacts of ZIKV infection. A high infectious dose (1×10⁶ FFU per mouse) of ZIKV was administered intravenously. Control animals received a single dose of anti-IFNAR blocking monoclonal antibody and succumbed to lethal neurological pathology within 13 days. Immunocompetent mice exhibited motor impairment such as arthralgia, as well as ocular inflammation resulting in retinal vascular damage, and corneal edema. This pathology persisted 100 days after infection with evidence of chronic inflammation in immune-privileged tissues, demyelination in the hippocampus and motor cortex regions of the brain, and retinal/corneal hyperplasia. Anti-inflammatory transcriptional responses were tissue-specific, likely contributing to differential pathology in these organs. Pathology in immunocompetent animals coincided with weakly neutralizing antibodies and increased ADE among ZIKV strains (PRVABC59, FLR, and MR766) and all Dengue virus (DENV) serotypes. These antibodies were autoreactive to GBS-associated gangliosides. This study highlights the importance of longevity studies in ZIKV infection and confirms the role of anti-ganglioside antibodies in ZIKV-induced neuro-ocular disease.

ARTICLE HISTORY

Received 28 February 2020
Revised 19 May 2020
Accepted 23 May 2020

KEYWORDS

Flavivirus; Zika virus;
auto-antibodies;
neuro-ocular pathology

Introduction

Zika virus (ZIKV) is a mosquito-borne flavivirus discovered in 1947 in a rhesus macaque within the Zika Forest of Uganda. Outbreaks of human ZIKV were occasional until an epidemic in 2015 with more than 37,000 cases in the US and US territories, and more than 1 million in Latin America.¹

ZIKV can spread via multiple modes of transmission: transplacentally to developing fetuses, via breastfeeding to infants, to adults through sexual intercourse, or cutaneously via mosquito bite. Congenital Zika syndrome (CZS), associated with microcephaly and birth defects, has been demonstrated in infants of infected pregnant women,^{2–4} and more recent reports point to impaired visual and neurological development among infants born with CZS independent of microcephaly.^{5–7} Flaviviruses persist up to 6 months in immune-privileged compartments such as brain, eyes, and genitals after the virus has been systemically cleared.^{8–10}

While infected adults can end up with permanent ocular damage, such as macular degeneration and retinal edema, the most severe consequence of adult infections is Guillain-Barré Syndrome (GBS), a disease attacking the nervous system. GBS

initially manifests gastrointestinal and respiratory symptoms,¹¹ and as autoantibodies develop, symptoms shift to the notable motor/neural impairment hallmarks. Diagnostic criteria for GBS include progressive symmetric weakness of one or more limbs, hyporeflexia or areflexia, and a full progression within 4 weeks.¹² Recent studies suggest that ZIKV-induced GBS develops during the course of infection, and not post-infection, as commonly seen with other GBS-inducing pathogens, such as *Campylobacter jejuni*.^{13–15} While the role of T cells in GBS-associated demyelination and neuroinflammation has been well studied,^{16,17} there is limited information on the putative role of ZIKV-specific antibodies in initiating or sustaining these symptoms. These facets of GBS necessitate the use of animal models enabling the long-term study of ZIKV-induced pathology.

Commonly used murine models for ZIKV infection are deficient in type-I interferon (IFN) receptors (IFNAR^{-/-} such as A129/AG129 strains), as flavivirus infections are intricately linked to the host IFN response. These murine models are either deficient in IFN receptors,¹⁸ or IFN signaling is inhibited by blocking receptors with antibodies to facilitate susceptibility to infection and enable extreme viremia.^{19–21} Consistent with

human infections, ZIKV-infected IFNAR^{-/-} mice develop purulent ocular discharge with detectable viral RNA (vRNA) in lacrimal glands and tears, and active ZIKV virions in Müller glial cells and optic tract tissues,²⁰ with symptoms persisting after viral clearance.²¹ However, these animals do not survive beyond 10 days post-infection, which limits studies of long-term infectious impacts.

Previous studies investigating the molecular mechanisms by which ZIKV gain access to the eye and causes inflammation have revealed the role of retinal epithelial infections and cell death in allowing for ZIKV to cross the blood-barriers of immune-privileged tissues.^{22,23} These investigations are often limited to *in vitro* studies of human primary cells, or juxtapose cell culture studies with ZIKV infection in wild-type (WT) C57BL/6 and immune-compromised animals. Singh et al. provides a thorough analysis of transcriptional responses after intravitreal inoculation of ZIKV into either WT or ISG15 deficient animals and shows a rapid induction of inflammatory responses during ZIKV infection.²² These findings coincide with retinal lesions and chorioretinitis that present within 24 hours of infection and last up to 96 hours after infection. While this insight into ZIKV pathogenesis of immune-privileged tissues is beneficial, the mechanism behind systemic ZIKV entry into the eye and ZIKV infection synergy between eye and brain remain to be determined.

In this study, immunocompetent BALB/c mice were intravenously infected²⁰ with a high dose of ZIKV-PRVABC59 suitable for this model.²⁴ BALB/c mice were selected over C57BL/6 mice for their ability to generate robust humoral responses and their use in vaccination studies. Similar studies in C57BL/6 mice require intracranial or intravitreal injection in order to achieve similar ZIKV neuro-ocular pathology.^{22,25} This study seeks to build on previous studies by examining the development and convalescence of neuro-ocular pathology over 120 days using a less traumatic form of inoculation. To assess infection-induced pathology, we adapted two ocular reflex assessments, and two motor/neural and joint tests. We evaluated the magnitude and quality of immune responses after infection.

Methods and materials

Cells and virus stocks

Vero cells (ATCC, CCL-81) for virus propagation and titration were maintained in DMEM (Mediatech, 10-013-CV) containing 10% fetal bovine serum (FBS; Hyclone, Thermo Scientific, SH3007103), 5% HEPES (Corning, H3537) and 1% Penicillin/Streptomycin (Corning, 30-002-CI). ZIKV stocks were generated from the African lineage Uganda strain (MR766, B.E. I. resources, NR-50085) and the Asian lineage, Caribbean isolate from Puerto Rico (PRVABC59, generously provided by Dr. Scott Michael and Dr. Sharon Isern at Florida Gulf Coast University). The FLR strain from Colombia was obtained from B.E.I resources (NR-50183). Dengue virus strains (DENV1/Hawaii/1944, DENV2/16681/Thailand/1964, DENV3/H87/Philippines/1956, and DENV4/UNC4019/Colombia/2006) were generously provided by Dr. Joshy Jacob of Emory University. All viruses were propagated in Vero cells for

7 days at 37°C. After the tenth passage, culture supernatants were collected and cell debris was cleared by centrifugation at 3,000xg for 10 minutes at 4°C. Viral harvest was then filtered using 0.22-micron filters (Sigma, Z741966). Culture supernatants were concentrated using Amicon centrifugal concentration filters (EMD Millipore, C7715) by centrifugation at 4,000xg for 30 minutes. As the ZIKV virion is approximately 50 nm in diameter, we used the 100 NMWL variant filters to maximize the recovery. Finally, viral supernatants were purified by discontinuous 20–60% sucrose gradient, where they were diluted 1:5 with FBS before final storage at –80°C.²⁶

Virus titration

Viral stocks were titrated by plaque assay performed in Vero cells as previously described.²⁷ Focus-forming assays were performed as previously described.²⁸ Blue foci were counted, and titers were calculated by foci numbers in infectious volume (# of foci x infectious volume x conversion factor to ml x dilution factor). FFU and PFU are equivalent in that both are quantification methods. In this study, PFU assays and FFU assays resulted in similar titers.

Trans-well focus-forming assay

To evaluate if live virus can be isolated from systemic and privileged tissues and bodily fluids, we adapted a trans-well infectious system similar to a monocyte chemotaxis assay used for Japanese Encephalitis Virus.²⁹ Tissue homogenates and cell suspensions were then added onto 0.4 μm trans-well insert systems (Corning, CLS3396) overtop sterile Vero cells. Live virus released from cells in contact with the insert filtered through the membrane to infect permissive Vero cells growing as a monolayer in the lower well. This provided a measure of tissue-specific live viral load as opposed to quantifying the amount of vRNA present in tissues.

Animal strains and housing

Female BALB/c mice (Charles River Laboratories) were housed in a biosafety level 1 facility at Emory University's Division of Animal Resources and viral infection experiments were performed on animals housed in a Biosafety Level 3 facility at Emory University's Division of Animal Resources. All experiments were conducted in accordance with protocols approved by Emory University's Institutional Animal Care and Use Committee (IACUC) in accordance with guidelines with the United States Federal Animal Welfare Act (PL 89-544) and subsequent amendments.

Animal infection, tissue and biological fluid sampling

Mice were infected with 1×10^6 FFU of ZIKV-PR virus intravenously (IV).³⁰ Serum or platelet-poor plasma (PPP) was collected 0, 3, 6, 10, 30, 40, 60, 80, 100, and 120 days post-infection; plasma was collected in citrate buffer and stored at –20°C until use. Small groups of mice were euthanized at the same time points and tissues were collected and processed for histology or, homogenized in protease inhibitors and RNase inhibitors (ThermoFisher Scientific, Waltham, MA) for infectivity and

qRT-PCR studies. In the remaining mice, tears were collected via PBS gavage 100 DPI and after euthanasia. Tissues (brain, eyes, genital organs, liver and spleen) were collected and processed for infectivity experiments, histology, and inflammatory markers. Ocular tissues were not perfused prior to harvest to avoid structural and cellular changes induced by the perfusion process,³¹ as functional morphology of the retina correlates directly with fluid pressure in the choroid. For both FFA and qRT-PCR quantification methods, tissues were homogenized after mincing and passaged through 40 μm cell strainers (Fisher Scientific, 08-771-1). They were further digested with 1 mg/ml of Collagenase IV (Worthington, LS004189) for 30 minutes at 37°C, and the purified through 40 μm cell strainers. Homogenates were separated using a Percoll (Millipore Sigma, P1644) density gradient,^{32,33} and cell suspensions were isolated for qRT-PCR and FFA trans-well studies. One eye from each animal was used for FFA and qRT-PCR experiments, and the other was used for tissue sectioning for microscopy studies.

Anti-IFNAR administration

Immunocompetent mouse infections were compared to a second cohort of animals that which received a one-time administration of anti-mouse IFNAR-1 functionally blocking monoclonal antibody (mAB) (MAR1-5A3, Leinco Technologies, #I-401). Each mouse received 1 mg of anti-IFNAR mAB via intraperitoneal injection 24 hours prior to infection.³⁴ The projected half-life of this dosage is 2.6 days.

RNA isolation and qRT-PCR

Total RNA was extracted from tissues using Trizol (Ambion, 15596018). Tissues were homogenized into Trizol reagent using the FastPrep-24 5 G homogenizer (MP Biomedicals). Total RNA was isolated using the PureLink RNA mini-kit (Ambion, 12183025). Purified RNA was quantified, checked for quality assurance, and then reverse transcribed with the qScript Reverse Transcription kit (QuantaBio, 95047). For quantification of vRNA, a standard curve was generated using 10-fold serial dilutions of ZIKV RNA standard. qRT-PCR for ZIKV prM-E was performed with TaqMan Gene Expression Master Mix, ZIKV Primers, and probe as previously described.³⁵ The standard curve had an R value greater than 0.99. vRNA copies were interpolated from the standard curve using the average Ct value obtained from samples run in triplicate. qRT-PCR for GAPDH, IL-1 β , TNF- α , IL-10, SOCS3, MMP2, MMP9, and COX2 were performed with Perfecta SYBR Green SuperMix Low Rox (Quantabio, #95056-500). Primers for GAPDH, IL-1 β , TNF- α , IL-10, SOCS3, and COX2 were as previously described.³⁶ MMP2 primers were as follows; forward 5'-AACGGTTCGGGAATACAGCAG-3'; reverse 5'-GTAAACAAGGCTTCATGGGGG-3'. MMP9 primers were as follows; forward 5'-AACCTCCAACCTCAGGACA-3'; reverse 5'-AGGTTTGGGAATCGACCCACG-3'. Data was analyzed using the $\Delta\Delta\text{Ct}$ method to determine normalized relative expression.

Ocular and brain symptomatology

At the same time points of blood collection post-infection, animals were assessed for ocular and motor/neural symptomatology. Behavioral tests to characterize pathogenesis in our mouse model were adapted from the Department of Molecular & Comparative Pathobiology's 2015 Lab Manual from Johns Hopkins University School of Medicine.³⁷ These assessments were identified and further researched with the explicit aim to evaluate visual and motor function following ZIKV infection.

Visual placement reflex

A reaching reflex test, or visual placement assessment, measures optic function and can also potentially indicate inflammation in parietal and occipital lobes of the brain.^{38,39} It is performed by holding the mouse gently by the tail suspended approximately 1–2 feet above a solid cage grate surface.³⁷ The mouse is then vertically lowered slowly toward the grate, taking note not to allow whiskers to contact the surface. A mouse with normal, average visual capabilities will attempt to reach toward the surface. A mouse that is blind, with impaired vision, or spatio-temporal problems will not attempt to reach until the whiskers contact the surface. Alternatively, the impaired mouse may also try to bend backwards on itself, in attempt to right itself using its awareness of gravity.

Palpebral reflex

Alternatively called the corneal reflex, it measures optic function and indicates potential inflammation in central nervous tissue connected to the optic tract, such as the trigeminal nerve, occipital lobe, and parietal lobes of the brain.^{40,41} It is performed by using a teased-out cotton tipped applicator. The mouse is held steady, and the cotton is gently touched against the cornea.³⁷ The blinking response is assessed on a scale of 0 to 3. On this scale, 3 represents a hyper-repetitive blinking in response to corneal stimulation; 2 equivocates to a normal, quick blink response; 1 corresponds to a slow blink or a closure response to stimuli; and a score of 0 indicates there was no response to corneal stimuli. Impaired or absent reflex responses suggests deteriorated motor/neural capabilities, eye function, and potential neurological inflammation.

Rear limb withdrawal

The limbic withdrawal test measures motor neuron responses in mice, and can indicate arthralgia in limb joints, and/or inflammation of motor neurons.^{42,43} The mouse is allowed to grip onto a surface and steadied by the tail.³⁷ One of the hind limbs is gently picked up and pulled taut at a 45° angle. The limb is then released, and the withdrawal of the limb is scored on a scale 0 to 3. On this scale, 3 represents a hyper-active response; 2 equivocates to a normal quick withdrawal of the limb back to normal position; 1 corresponds to a slow response to stimulus; and a score of 0 indicates no response, with the leg dropping to the ground and not returning to normal position.

Grip time assessment

The grip time assessment quantitatively evaluates mouse muscular capabilities and indicates potential arthralgia and muscular coordination issues.^{44,45} The test was performed by placing a mouse on a grated cage lid, and the grate was suspended 1–2 feet above the bench-top or cage.³⁷ The mouse and grate were gently shaken for 1 minute, and then rapidly inverted to bring the mouse into an upside-down position. The time the mouse could successfully hold on without falling off the grate was recorded. Healthy mice are expected to be able to hold onto the grate for a minimum of 1 minute. Any recordings less than 60 seconds was considered abnormal.

Histopathology and immunofluorescence of eyes and brain

To evaluate tissue infectivity, viral burden, and infection-induced histopathology; eyes and brains were harvested from 5 out of 20 total mice per group at 10 DPI and the remaining 15 mice at 100 DPI. The tissues were fixed in 10% formalin solution, followed by paraffin embedding for 8 μ m sectioning. Sectioning of brain tissues was performed at the Neuropathology/Histochemistry core of the Emory NINDS Neurosciences Core Facility (P30 NS055077), sectioning and H&E staining of eye tissues was performed by the L.F. Montgomery Ophthalmology Pathology core.

Immunofluorescent staining

Slides were de-waxed and rehydrated using sequential washes of xylene, ethanol, and distilled water. Antigens were unmasked and retrieved by submersion in sodium citrate buffer (10 mM, pH 6.0) for 10 minutes at 56°C. Aldehyde auto-fluorescence was quenched in a humidified chamber using 3 M glycine solution, and lipofuscin auto-fluorescence was quenched using Sudan-Black B. Slides were then blocked in bovine serum albumin (2% BSA)-TBS. Primary antibody diluted in 1% BSA in PBS buffer was added directly on top of each section, and slides were incubated overnight at 4°C. The 4 G2 antibody (Millipore, MAB10216) was used for viral infectivity analysis. Myelination studies utilized anti-MBP-Alexa Fluor488 (SantaCruz, sc-271524), anti-Vimentin (Rabbit anti-Mouse, Abcam, ab92547), and anti-Myelin PLP (Rabbit anti-Mouse, Abcam, 28486) antibodies. Secondary antibodies were fluorescently conjugated (Anti-Mouse Alexa594, Biolegend #405326; Anti-rabbit Alexa547, Abcam, ab150167; Anti-mouse Alexa488, Invitrogen, A10667), diluted in 1%BSA in PBS solution and incubated for 2 hours at room temperature. Prolong Gold Antifade mounting medium with DAPI (Thermo-Fisher, P36931) was applied, and slides were covered with a coverslip. Images were taken on Zeiss AxioScope microscopes via SPOT-advanced imaging software. Images were processed in Fiji/ImageJ.

TUNEL staining

TUNEL stain was selected because it identifies infection-induced cell death via DNA fragmentation irrespective of specific cell death pathways i.e.apoptosis, necroptosis, or pyroptosis.^{46–48} Terminal deoxynucleotidyl transferase dUTP nick end labeling, or TUNEL, staining was performed

according to manufacturer protocol (Abcam, ab66110). Slides were de-waxed and rehydrated using sequential washes of xylene, ethanol, and distilled water. Antigens were unmasked and retrieved by submersion in sodium citrate buffer (10 mM, pH 6.0) for 10 minutes at 56°C. Aldehyde auto-fluorescence was quenched in a humidified chamber using 3 M glycine solution, and lipofuscin auto-fluorescence was quenched using Sudan-Black B. Slides were then blocked in bovine serum albumin (2% BSA)-TBS. Slides were then washed in PBS and blocked using a proteinase K solution for 5 minutes at room temperature. Wash slides with PBS and then label fragmented DNA using TdT enzyme, enzyme buffer, and Br-dUTP (Abcam, ab66110). Prolong Gold Antifade mounting medium with DAPI (Thermo-Fisher, P36931) was applied, and slides were covered with a coverslip. Images were taken on Zeiss AxioScope microscopes via SPOT-advanced imaging software. Images were processed in Fiji/ImageJ.

Quantification of MBP, Myelin PLP, and 4G2 positive cells

Corrected total cellular fluorescence (CTCF, also called normalized MFI) was determined as described by Lourenço et al. for both MBP, myelin PLP, and vimentin stains.⁴⁹ Similarly, to determine the percentage of 4G2 positive cells, DAPI foci and 4G2 cells were enumerated both manually and automatically, using the “Threshold” and “Analyze particles” functions in FIJI/ImageJ. The percent of infected cells was then calculated as the number of 4G2 positive cells was divided by the number of DAPI positive foci.

Antibody titration and characterization

ELISAs

Anti-ZIKV specific antibodies were determined by coating flat bottom, 96-well Nunc MaxiSorp plates (Thermo-Fisher, 44–2404–21) with 4 μ g/ml of inactivated virus stocks, diluted in sodium bicarbonate buffer. Plates were incubated overnight at 4°C, washed with PBS-Tween 0.5% and blocked with 2% BSA in PBS for 1 hour. Individual PPP samples were run in duplicate and incubated for 2 hours at 37°C. The standard curves were generated with appropriate purified mouse immunoglobulins and isotype-specific HRP-labeled detection antibodies (Southern Biotech, Birmingham, AL). Sample IgG concentrations were determined by interpolation from standard curves. Anti-ganglioside specific antibody concentrations were determined similarly. Flat bottom, 96-well Nunc MaxiSorp plates were coated with 2 μ g/ml of either GD1a, GD1b, or GT1a ganglioside (SantaCruz, sc-202621, sc-202622, sc-202629, respectively). Standard wells were coated as described above. PPP samples were diluted. Standard curve antibodies and development of plates was performed as described previously.⁵⁰

Focus-forming reduction by neutralization assay (FFRNT)

Heat-inactivated PPP samples were diluted serially and combined with 100 FFU live virus. Antibody dilutions and virus were co-incubated for 1 hour at 37°C, and then added over Vero cells for 24 hours. The focus-forming assay was performed as described.²⁸

Antibody-dependent enhancement assay

ADE assay protocol was performed as described using U937 cells.²⁸ The cells were maintained in suspension in complete RPMI medium. Cells were stained with 4G2 antibody (EMD Millipore). Samples were run on a CytoFLEX LX system at Pediatrics/Winship Flow Cytometry Core of Winship Cancer Institute of Emory University, Children's Healthcare of Atlanta and NIH/NCI, which is supported under the award number P30CA138292.

Statistical analysis

Correlation analysis was performed on vRNA titers determined by qRT-PCR for brain and eyes to determine a relationship with raw reflex scores. Pearson's correlation coefficient with a two-tailed *p*-value were calculated for each of the four reflexes. For ELISA assays, linear regression tests to interpolate OD values into concentrations. For co-culture assays and qRT-PCR, two-way ANOVA was used to analyze differences between infected and uninfected infections were followed by Sidak's Post Hoc test for multiple comparisons. Two-way ANOVA with Sidak's post-hoc was also used to determine differences between uninfected and infected groups. For immunofluorescence assays, two-way ANOVA was used to compare differences in hippocampal and cortical regions, as well as between early and late time points. Non-linear regression analysis was performed to determine the IC₅₀ (95% confidence interval) for avidity and neutralization assays. A *p*-value less than 0.05 was considered significant.

Results

ZIKV-PRVABC59 infection in immunocompetent mice results in distinct neurological and ocular pathology

Current mouse models for ZIKV are insufficient for long-term studies because they utilize low infectious dosages (less than 1×10^3 FFU) to generate acute pathology and mortality within 1 week of infection. When immunocompetent animals were infected with 1×10^6 FFU of virus, symptoms and pathology typical of ZIKV infections presented within 3 days post infection (DPI). While the moribund weight loss of 25% or greater seen in IFNAR^{-/-} models was not observed, infected BALB/c mice lost 10% of their starting weight by 6 DPI, and never recovered to match uninfected animals (Figure 1A). To evaluate how immunocompetent BALB/c mice compare to similar immune compromised models, we administered 1 mg of anti-IFNAR mAb by intraperitoneal injection 24-hours prior to infection. These animals lost approximately 20% of their initial body weight, and were euthanized due to seizures at 3, 4, 5, 10, 11, and 12 DPI (Figure 1B). Only 1 animal the received anti-IFNAR block survived beyond 12 DPI.

ZIKV has demonstrated persistence in human organs and fluids for ≥ 200 days.⁵¹ Thus, we quantified viral burden in tissues and secretions with a focus-forming assay (FFA) co-culture, where homogenized tissues were used in a trans-well system over permissive Vero cells. Homogenized tissues would then shed live virus through the membrane pores, infect permissive sterile cells below, and where the readout

of this assay is FFU/ml. Homogenates were not added directly to monolayers because it does not discriminate if the cells are permissive to infection or a productive infection. Previous concerns were raised that ZIKV would not propagate in WT BALB/c tissues due to STAT non-homology. Thus, they were evaluated here to specifically identify if live virus was being shed from the tissues. Among immunocompetent mice, the maximum viral load in systemic organs was similar, between 1.4×10^4 and 1.3×10^4 FFU/ml in liver and spleen. Mice which received anti-IFNAR treatment showed a maximum of 2.2×10^4 and 1.9×10^4 FFU/ml in these same tissues (Figure 1C). Viral burden in their immunoprivileged tissues, eye and brain, were 1.3×10^4 FFU/ml and 9.3×10^3 FFU/ml, respectively. In contrast, anti-IFNAR recipients showed a maximum of 1.8×10^4 and 1.7×10^4 FFU/ml in identical tissues. Viral load in immunocompetent animals was 1.7-fold greater in plasma vs tears. Among anti-IFNAR mice, tears exhibited an average of 1.7×10^4 FFU/ml and plasma a maximum of 2.9×10^4 FFU/ml (Figure 1C). To correlate live virus isolations to the amount of vRNA present within immunoprivileged tissues, qRT-PCR was performed at 10 and 100 DPI in brain, eyes, and plasma in both immunocompetent and immunocompromised mice and showed that anti-IFNAR administration resulted in elevated viral load in all tissues (Figure 1D). Animals that received anti-IFNAR injection demonstrated a maximum vRNA concentration of 1×10^4 , 7.1×10^3 , and 1.7×10^4 ng/ml in brain, eyes, and plasma respectively. Immunocompetent animals demonstrated maximum infectivity levels of 5.8×10^3 , 4.2×10^3 , and 1×10^4 ng/ml of vRNA in the same tissues, respectively.

Our model demonstrated vision and motor-function abnormalities following ZIKV infection similar to those observed in human infections and in other published IFNAR^{-/-} murine models.⁵² We standardized palpebral and visual placement reflex tests to evaluate ocular pathology and intracranial inflammation, and rear-limb withdrawal and grip tests to evaluate motor/neural pathology. Palpebral reflex deficits can indicate inflammation in facial, ocular, and cranial nerves.^{53,54} Among infected immunocompetent mice, 55% lost normal palpebral reflex responses 3 DPI. Symptoms reached their nadir 6 DPI, where 75% of mice exhibited aberrant or loss of normal reflexes (*p* < .0001 for all time-points) (Figure 2A). Palpebral reflexes appeared to recover in 60% of the animals in the remainder of the time-course, whereas 40% of mice demonstrated a persistent loss of normal reflexes until the end of monitoring period (120 DPI). Among anti-IFNAR mice, palpebral reflexes declined within 3 DPI, reaching a nadir where all animals had lost palpebral/corneal reflexes 30 DPI. This loss persisted up to 120 DPI (Figure 2A).

Visual placement reflex deficiencies can suggest abnormalities in optic and cranial nerve function. For this assessment, hyporeflexia indicates an animal's reflexes are reduced or slowed to a debilitating degree. Similar to palpebral reflex kinetics, hyporeflexia in immunocompetent mice was observed as early as 3 DPI, and appeared to reach a nadir between 6 and 10 DPI where 50% of all animals demonstrated loss of visual placement reflexes (*p* < .0001 for all time-points) (Figure 2B). Thirty percent of mice demonstrated persistent hyporeflexia 120 DPI, indicating non-resolving neurological/ocular

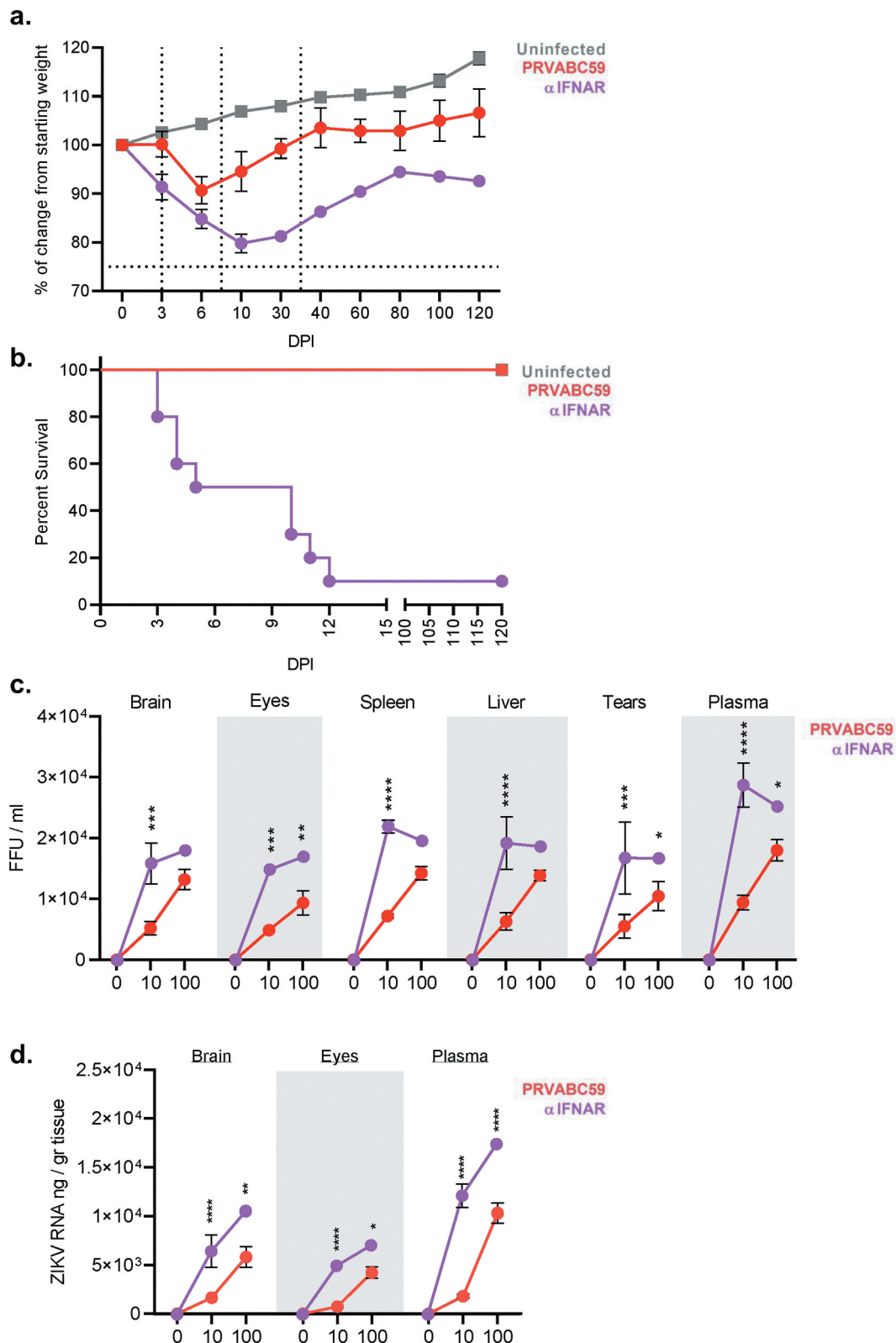


Figure 1. PRVABC59 can infect systemic and privileged organs in immunocompetent mice. (A) Body weight changes were monitored for 120 DPI. (N = 10). PRVABC59 infected mice were immunocompetent, while mice denoted as α IFNAR (anti-IFNAR) received a single administration of monoclonal antibody that functionally blocks IFNAR signaling 24 hours prior to infection. The N for α IFNAR mice decreased from 10 to 5 between 3 and 6 DPI, and further decreased from 5 to 1 between 10 and 30 DPI. These losses are denoted by vertical lines. The horizontal dotted line represents lethal weight loss endpoint. (B) Survival of mice infected with ZIKV with and without prior administration of α IFNAR mAb. (C-D) Active viral replication was determined by infectious co-culture (C) at 0, 10, and 100 DPI. Total ZIKV genomic RNA was quantified by qRT-PCR (D; N = 5) at 0, 10, and 100 DPI. For panels C and D, N = 3 at 0 and 3 DPI, and for PRVABC59 group at 100 DPI. N = 1 for α IFNAR at 100 DPI. All error bars in all panels reflect Standard Deviation. Data was analyzed by Two-way ANOVA using Sidak post-hoc correction. For all panels, * is $p < .05$, ** is $p < .01$, *** is $p < .001$, and **** is $p < .0001$.

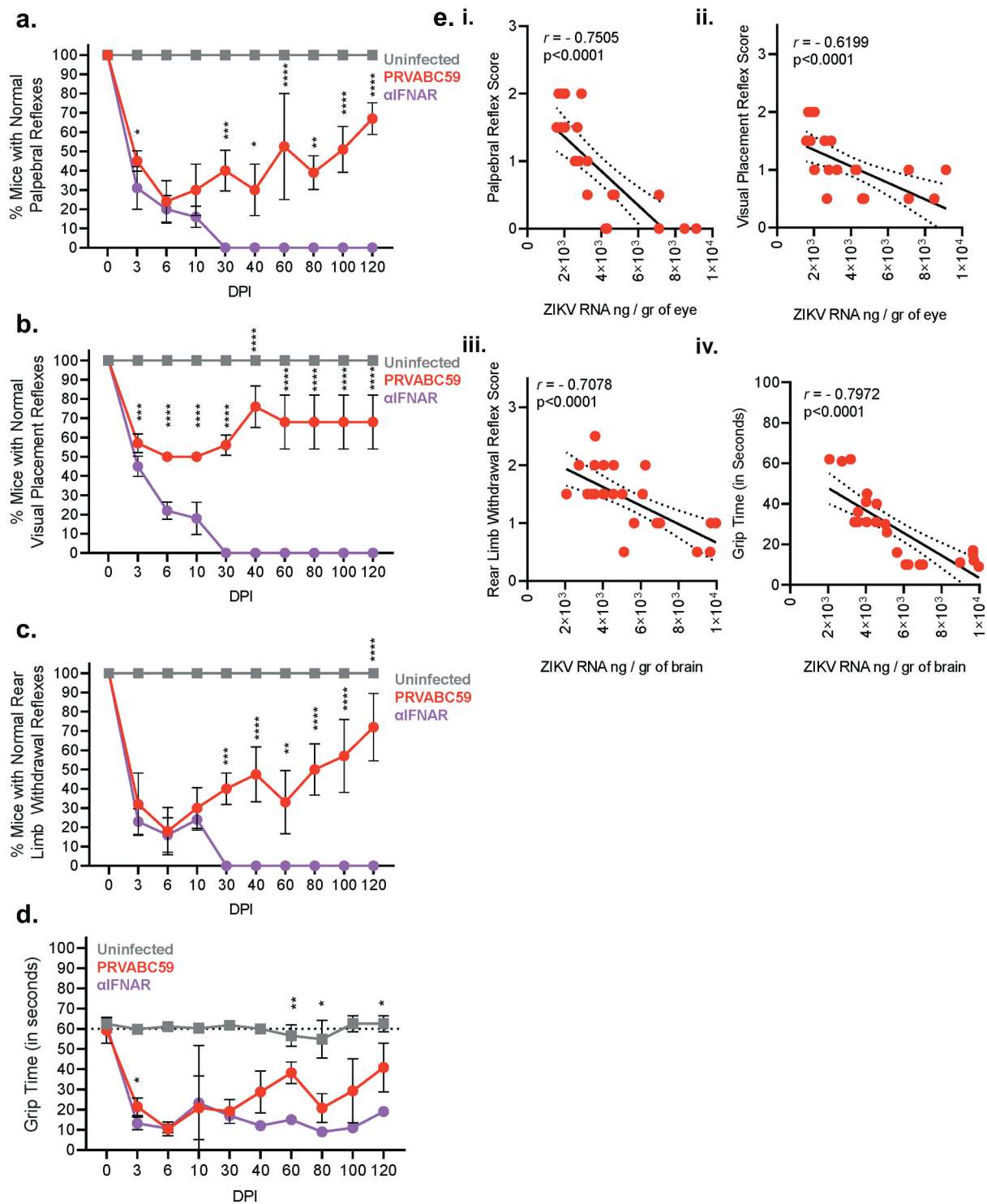


Figure 2. Competent mice infected with ZIKV-PRVABC59 demonstrate distinct ocular and motor/neural symptomatology that correlate with viral load. Ocular clinical scores were determined via palpebral (A) and visual placement (B) reflexes. (Two-way ANOVA with Bonferroni's post-hoc correction; $N = 10$). Motor/neural clinical scores were evaluated by rear-limb withdrawal reflex tests (C) and by grip time tests (D). The dotted line among grip time tests indicates the standard time a healthy animal should endure test conditions. (Two-way ANOVA with Bonferroni's post-hoc correction; $N = 10$). (E) Symptom severity and viral load at 100 DPI in the affected tissue were analyzed by Pearson's test to determine potential correlations for palpebral (i), visual placement (ii), and rear limb withdrawal reflexes (iii) and for grip time tests (iv). Dashed lines represent 95% confidence interval bands; Pearson's correlation coefficient and p -values are listed for each graph. All correlation analyses used infectious and symptom data ($N = 25$). For all panels, * is $p < .05$, ** is $p < .01$, *** is $p < .001$, and **** is $p < .0001$. All error bars in all panels reflect standard deviation.

infectious sequelae. Among anti-IFNAR mice, the remaining animals demonstrated hyporeflexia at 30 DPI which persisted until 120 DPI.

Rear-limb withdrawal reflexes assess joint pain, inflammation, and motor/neural pathology. Among immunocompetent

infected mice, 70% lost normal withdrawal reflex 3 DPI. Symptoms reached their nadir 6 DPI, where 80% of mice exhibited aberrant or loss of withdrawal reflex ($p < .0001$ for all time-points) (Figure 2C). Reflexes among this cohort appeared to recover across the remainder of the time-course

with a notable relapse 60 DPI. At 120 DPI, 30% of mice demonstrated a persistent loss of withdrawal reflexes. Anti-IFNAR animals exhibited a constant and steady decline of withdrawal reflexes until the remaining animal because unresponsive at 30 DPI (Figure 2C).

Similar to rear limb withdrawal assessments, immunocompetent mice evaluated via grip time demonstrated motor/neural impairment as early as 3 DPI, evident by the 2.7-fold reduction in average grip time of infected animals. Hyporeflexia reached the nadir 6 DPI, with a 5.8-fold reduction in average grip time ($p < .0001$ for all time-points) (Figure 2D). While symptoms appeared to convalesce, a secondary drop in grip time occurred between 60 and 80 DPI, potentially indicating a periodicity of symptoms or recurrence of infection. The average grip time among infected mice remained 35% lower than uninfected animals 120 DPI. Anti-IFNAR treated animal showed an immediate decline in grip abilities that persisted and did not recover through 120 DPI.

Correlation analyses were performed to determine the relationship between viral burden and reflex clinical assessment scores 100 DPI in immunocompetent mice (Figure 2E). Palpebral and visual placement clinical assessments primarily evaluate ocular functionality, pain, and inflammation. Scores from these tests were plotted against the concentration of ZIKV RNA per gram of eye tissue as determined by qRT-PCR. Both palpebral and visual placement scores demonstrated a strong negative correlation (palpebral $r = -0.7505$ and $p < .0001$; visual placement $r = -0.6199$ and $p < .0001$) between increasing viral load and ocular reflex scores (Figure 2E-i and ii). Rear limb withdrawal and grip time tests were used to evaluate motor/neural inflammation, function, and pain. Scores from these two clinical assessments were plotted against the concentration of ZIKV RNA per gram of brain tissue as determined by qRT-PCR. Rear limb withdrawal and grip time evaluations both exhibited a strong negative correlation between increasing viral load and decreasing motor/neural responses (withdrawal $r = -0.7078$ and $p < .0001$; grip times $r = -0.7972$ and $p < .0001$) (Figure 2E-iii and iv). Collectively, these data demonstrated that immunocompetent mice infected with high doses of ZIKV, suffered from mild weight loss and reduced recovery resulting in distinct neurological and ocular pathology that significantly correlated with viral burden.

ZIKV infection-induced antibodies have limited cross-protection and enhance infection among ZIKV and DENV strains

To characterize and evaluate kinetics of ZIKV-specific IgG antibody subtype production and evaluate antibody maturation progression, we collected PPP up to 120 DPI from immunocompetent mice. ZIKV-specific IgG total concentrations were low within the first 40 DPI, never exceeding 77 ng/ml. After 40 DPI, IgG total concentrations increased until 80 DPI, where they plateaued at 647.5 ng/ml and reached a maximum of 714.1 ng/ml (Figure 3A). ZIKV-specific IgG1 concentrations never exceeded 116.8 ng/ml

during the length of the study (Figure 3B), and IgG2a concentrations demonstrated increasing titers until 60 DPI, with a maximum of 110.3 ng/ml followed by a sharp spike in concentrations reaching a maximum of 332.2 ng/ml (Figure 3C). This data demonstrates that there was a sharp increase in antibody titers around 60 DPI, and that the majority of these antibodies were IgG2a.

As antibody cross-reactivity has been well documented between ZIKV and DENV, we next aimed to characterize antibody quality, based on the ability to neutralize ZIKV strains and DENV serotypes, and to potentiate infection of non-permissive cell types 100 DPI. Neutralizing virus titer was determined using a contemporary South American ZIKV strain from Colombia, FLR; and an ancestral African lineage strain from Uganda, MR766 (Figure 3D). Of ZIKV strains, PRVABC59 demonstrated 50% neutralization at a titer of 628, while neither FLR nor MR766 demonstrated neutralization beyond a titer of 16. Four DENV strain serotypes were selected for neutralization analysis (Figure 3E). Of these four serotypes, only DENV-1 and DENV-2 exhibited antibody-mediated neutralization with titers of 61 and 33, respectively. This data demonstrates that antibodies generated by ZIKV infection were specific to the strain of infection, and had little to no neutralization capacity to other strains of ZIKV or to DENV serotypes.

Flavivirus antibody cross-reactivity is a double-edged sword; often antibodies can neutralize different viruses at high concentrations but also enhance infection via incomplete neutralization at lower concentrations. Antibody-dependent enhancement (ADE) is a well-studied phenomenon where poorly neutralizing antibodies against one flavivirus or virus strain can increase infectivity of another virus or strain.⁵⁵ Here, we evaluated the ability of antibodies generated against PRVABC59 to enhance infectivity of homologous and non-homologous ZIKV strains and DENV using non-permissive U937 cells that will only be infected by through ADE. Antibodies generated by ZIKV infection demonstrated some autologous neutralization capabilities at high antibody concentrations and became enhancing at a titer of 320. Among ZIKV strains, both FLR and MR766 demonstrated an endpoint titer of 40, which resulted in 92% and 86% of cells becoming infected, respectively (Figure 3F). Despite the lineage differences, FLR and MR766 infection is a direct product of antibody concentration as evinced by infectivity and antibody concentration decreasing simultaneously. This also points to potential differences among E-protein sequences where FLR and MR766 have a common sequence distinct from PRVABC59. Among DENV serotypes, DENV-2 and DENV-4 demonstrated similar peaks of infectivity at titers of 160 and 80, respectively, with a maximum of 85% of all cells infected for both viruses. DENV-1 infected 71% of all cells at an endpoint titer of 20, and DENV-3 exhibited 74% of cells infected at a titer of 320 (Figure 3G). The trend observed for DENV-1 ADE in (Figure 2G) demonstrates that virus neutralization is a product of antibody concentration and not epitope specificity, as ADE decreases as antibody concentration decreases. Collectively, these data demonstrate that antibodies generated by ZIKV infection were both poorly neutralizing and highly enhancing to non-homologous viruses and strains.

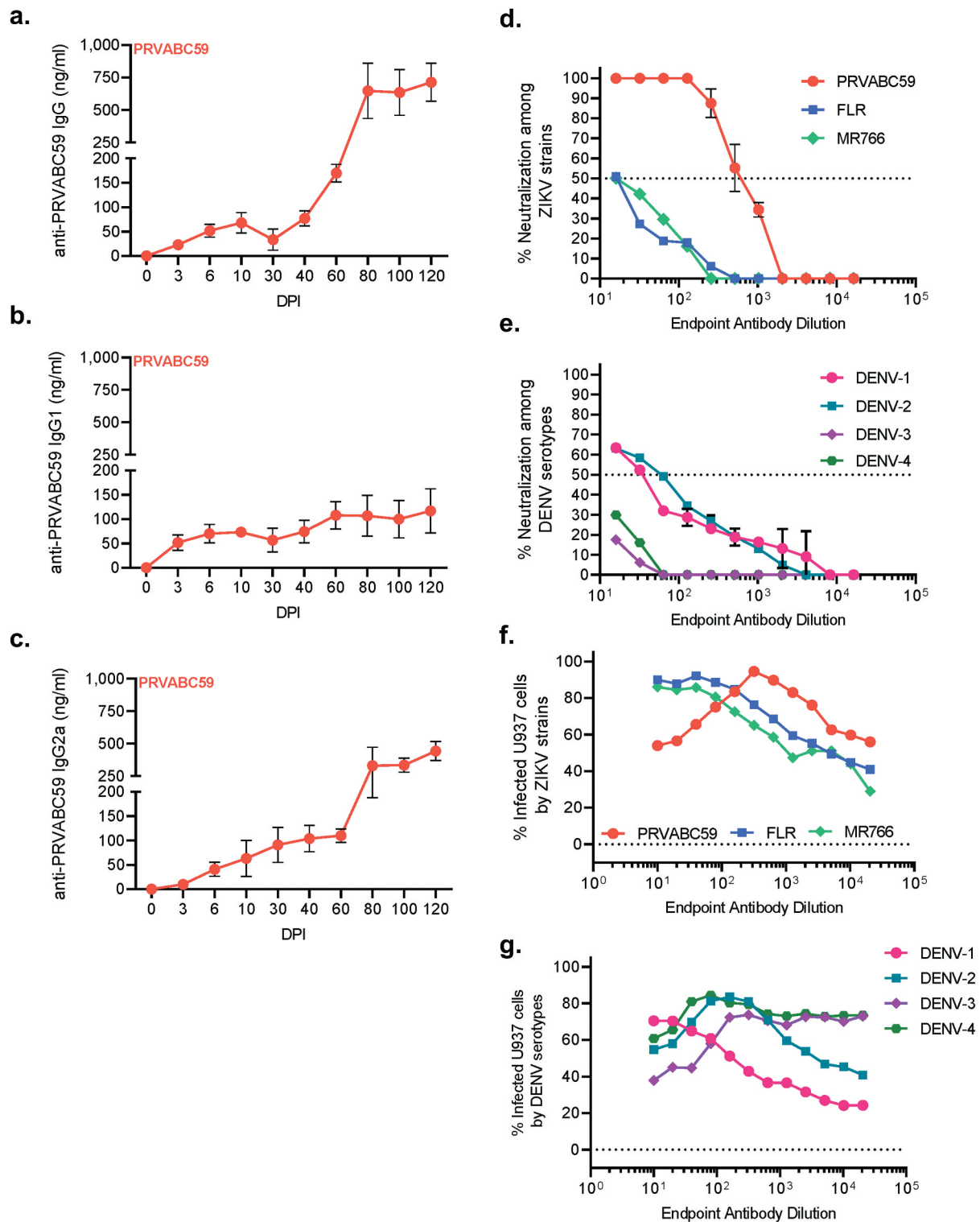


Figure 3. PRVABC59-induced antibodies are weakly neutralizing and enhance non-homologous infection. Antibody kinetics for IgG total (A), IgG1 (B), and IgG2a (C) that are specific to PRVABC59 were determined up to 120 DPI via ELISA using whole, inactivated virus particles. (N = 5). (D-E) Antibody neutralization was evaluated by determining the endpoint antibody titer necessary to neutralize 50% of live virus (IC_{50}) among homologous and non-homologous ZIKV strains (D; N = 5) and a representative strain from all four DENV serotypes (E; N = 5). The horizontal line indicates when 50% of live virus has been neutralized. (F-G) Antibody-mediated infection was evaluated among homologous and non-homologous ZIKV strains (F) and a representative strain from all four DENV serotypes (G; N = 5). Background fluorescence, denoted by the horizontal dotted line, was determined by combining virus, no antibody sample, and cells. All error bars in all panels reflect standard deviation.

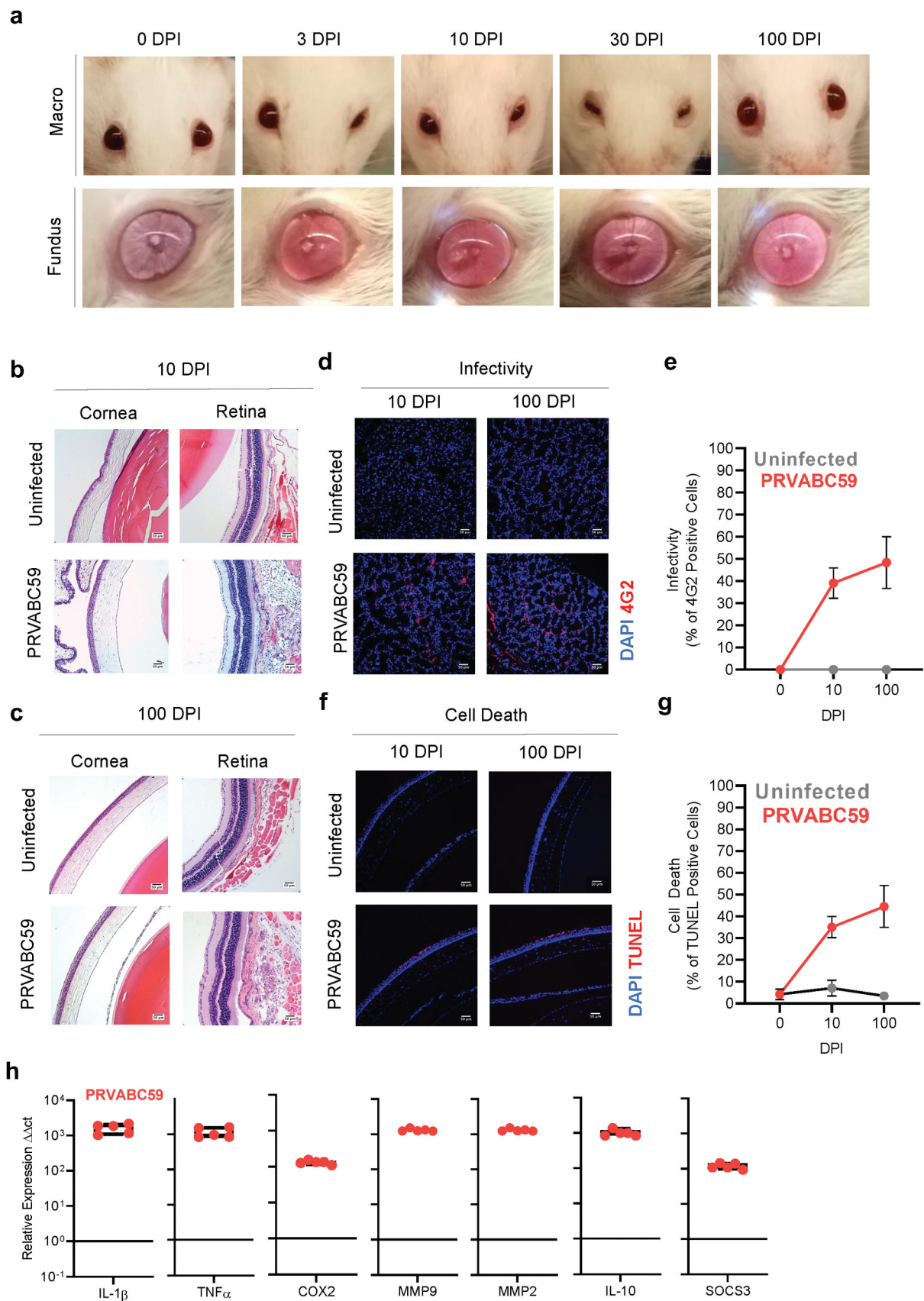


Figure 4. Tenacious corneal and retinal hyperplasia coincides with persistent ocular infection, increasing levels of cell death, and chronic inflammation. (A) Macroscopic (top) and fundus (bottom) imaging was done at 0, 3, 10, 30, and 100 DPI to visualize ocular pathology. (B-C) Eyes from infected and uninfected mice were harvested 10 (B) and 100 (C) DPI for H&E and immunofluorescent staining. H&E images of corneal and retinal layers were taken at 20x to assess pathology. (D-E) ZIKV infectivity was determined by immunofluorescent staining for flavivirus antigens (Two-way ANOVA with Bonferroni's post-hoc; N = 10). (F-G) Similarly, TUNEL staining for cell death was performed at 10 and 100 DPI (Two-way ANOVA with Bonferroni's post-hoc; N = 10). (G) qRT-PCR on pro-inflammatory proteins, pain mediators, MMPs, and anti-inflammatory proteins among infected brains were normalized to GAPDH and then to expression levels of uninfected controls using the $\Delta\Delta Ct$ method (N = 5). For all panels, * is $p < .05$, ** is $p < .01$, *** is $p < .001$, and **** is $p < .0001$. All error bars in all panels reflect standard deviation.

Corneal and retinal hyperplasia among infected mice coincides with elevated cell death and persistent inflammation in the eye

Conjunctivitis and uveitis are common symptoms among humans infected with ZIKV, and ocular pathology comparable to them has been observed in IFNAR^{-/-} mouse models of ZIKV pathogenesis.^{21,56} We documented macroscopic conjunctivitis by facial imaging of the same immunocompetent mouse across infectious time-points in effort to detail animal pain according to the mouse grimace scale^{57,58} (Figure 4A, top-row). Unilateral swelling and orbital tightening was evident 3 DPI and progressed to bilateral swelling with purulent discharge 10 DPI. Both eyes showed intense purulent discharge at 30 DPI, and swelling was persistent up to 100 DPI (Figure 4A, top row). Fundoscopy was performed simultaneously and showed intense vascular inflammation 3 DPI. Retinal edema and vascular inflammation developed 10 DPI, persisted up to 30 DPI, and was not fully resolved by 100 DPI (Figure 4A, bottom-row).

Eye tissues were sampled 10 and 100 DPI to determine infection-induced morphological changes during early and late stages (Figure 4B-C). Within 10 DPI, infected = mice demonstrated chemotic conjunctiva, minor edema of corneal epithelia, and increased leukocyte infiltration within corneal stroma (Figure 4B, left side). ZIKV infections also presented edematous retinal pigmented epithelial (RPE) layers which contributed to further retinal degeneration, and notable immune infiltration of sclera and ganglionic layers (evident by increased nuclei present in these layers) (Figure 4B, right-column). Through 100 DPI, animals showed non-resolving warping of corneal epithelia, and hyperplasia within the cuboidal and squamous layers (Figure 4C, left column), with persistent leukocytes within the stroma. Retinal layers of infected animals showed bifurcation of the ganglionic layer and distinct edema of RPE (Figure 4C, right-column).

Active virus and vRNA could be isolated from eyes of infected animals 100 DPI. Thus, we aimed to identify cell tropism within the eye, possible changes in tropism as infection progresses, and whether morphologically affected tissues demonstrated increased infection or infection-induced cell-death. Viral proteins were detected as early as 10 DPI in lacrimal glands and cornea of infected mice and persisted 100 DPI (Figure 4D; S2 A-B). The number of infected cells increased 1.2-fold between 10 and 100 DPI ($p = .006$) (Figure 4E). To quantify infection-induced cell death, we fluorescently labeled apoptotic and necrotic cells using terminal deoxynucleotidyl transferase dUTP nick end labeling (TUNEL); we and observed increased levels of cell death in cornea and lacrimal glands (Figure 4F; S2 C-D). When compared to uninfected animals, ZIKV-infected eyes exhibited 5-times higher cell death after 10 DPI, and 12.6-times greater levels of cell death after 100 DPI. Between 10 and 100 DPI, cell death within infected eyes increased 1.3-fold ($p = .004$), which correlated with the fluorescent infectivity data (Figure 4G).

IL-1 β and *TNF- α* transcription were 1611-fold and 964-fold greater in ZIKV-infected eyes compared to uninfected eyes (Figure 4H). *COX2* expression among infected eyes was 111-

times greater than in uninfected eyes. MMP transcription was also elevated, with *MMP2* showing 1,861-fold higher expression and *MMP9* exhibiting 1,313-fold increased transcription. Transcription of the anti-inflammatory cytokines *IL-10* and *SOCS3* was increased 1,007- and 108-fold respectively. Collectively, these data demonstrate that ZIKV infection-induced ocular hypo- and areflexia may be the manifestation of direct infection and cell death of eye tissues, which subsequently mediate leukocyte infiltration, tissue morphology changes, and pan-uveitis inflammation.

ZIKV infection reduces myelin expression and results in prolonged inflammation in the brain

We observed decreased neurological and motor reflexes and elevated concentrations of anti-ganglioside autoantibodies after infection of immunocompetent mice with PRVABC59. The severity of pathology correlated strongly with viral load in brain tissues, and the antibodies generated by infection were characterized as poorly neutralizing, broadly cross-reactive, and able to robustly induce infection in non-permissive Fc γ -R bearing leukocytes. These data in conjunction with established literature linking anti-ganglioside antibodies with aberrant myelin expression among GBS patients⁵⁹ led us to investigate ZIKV-induced myelin expression alterations in the brain. Murine tissues were harvested from immunocompetent 100 DPI and processed for immunofluorescent histochemistry using dual stains for pan-flavivirus group antigen and myelin glycoproteins common on myelin-bearing cells, such as oligodendrocytes and Schwann cells.

ZIKV infectivity immunofluorescence was performed to determine if viral antigen was isolated to specific regions of the brain; the total amount of infected foci were normalized against the total number of cells present in the optic field. Both the hippocampus and cortex showed 35–40% infectivity (Figure 5A). Myelin basic protein (MBP) and myelin proteolipid protein (mPLP) are the most abundant proteins in the CNS which contribute to the myelin sheath.⁶⁰ Thus, we stained brain sections for MBP in cortex sections, which revealed that infected mice had 2.5 times lower MBP expression than uninfected animals ($p < .0001$) (Figure 5B and C; S1A). Hippocampus and cortex regions stained for mPLP showed a 2.3- and 1.9-fold lower expression, respectively, compared to uninfected mice ($p = .0001$, $p = .001$) (Figure 5D-F; S1B and C). GBS patients have not only demonstrated antibody-mediated reduction in MBP and mPLP, but also a reduction in intermediate neuro-filament and glial cell body proteins, such as vimentin (Vim).⁵⁹ Hippocampus and cortex regions from infected animals demonstrated 2.1- and 2.0-fold less Vim expression compared to uninfected animals (both $p < .0001$) (Figure 5G-I; S1D and E).

Chronic inflammation plays a critical role in mediating the long-term consequences of GBS,⁵⁹ thus we characterized transcription of immune proteins 100 DPI from brains of immunocompetent mice. ZIKV infection increased *IL-1 β* and *TNF- α* levels by 500 and 660-fold, respectively (Figure 3). *IL-1 β* expression can be regulated by cyclooxygenase 2 (*COX2*), a pain mediator, via a positive feedback

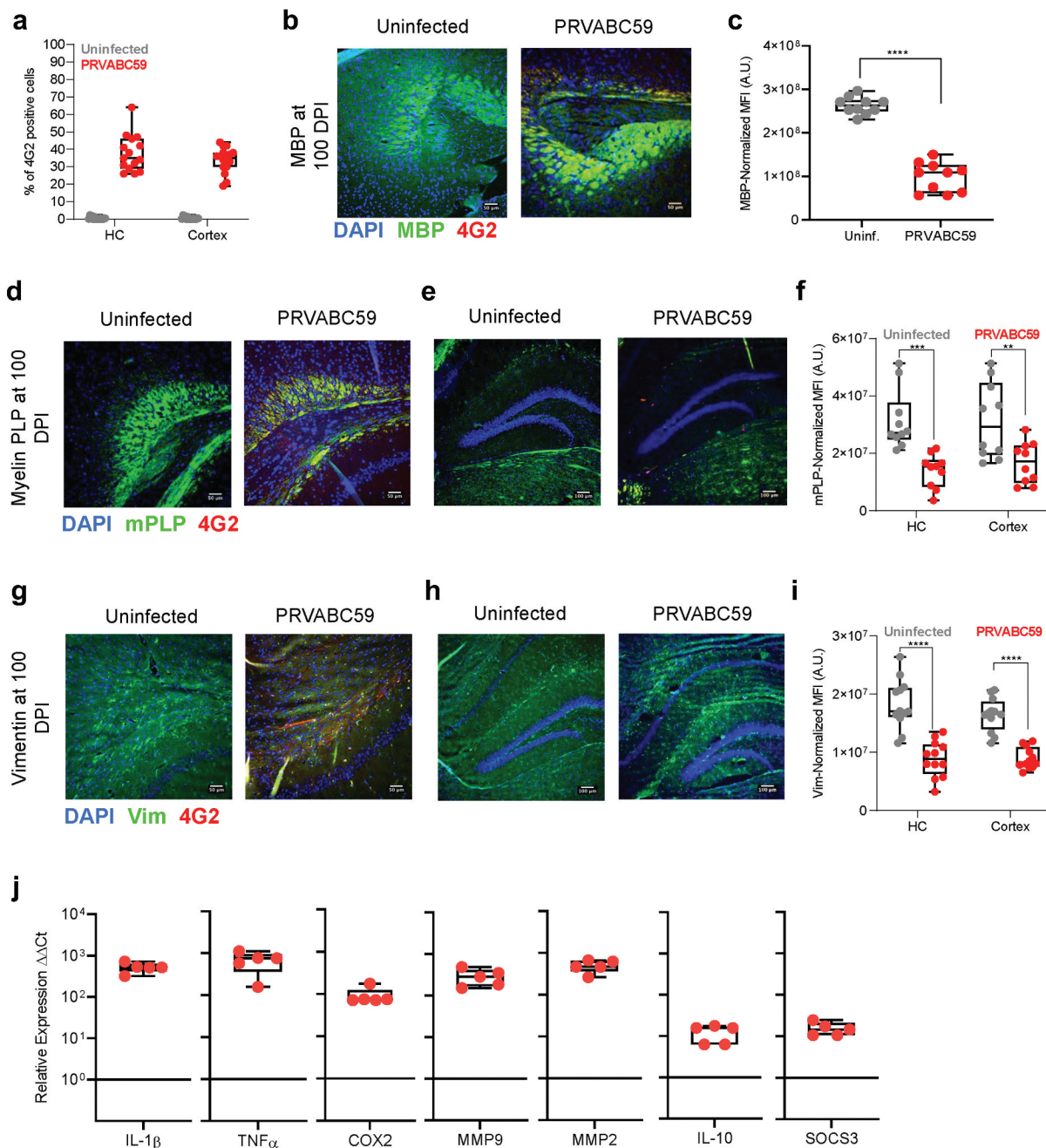


Figure 5. PRVABC59 infection in the hippocampus and cortex corresponds to decreased levels of myelin and persistent inflammation. (A) Brains were sectioned and stained for ZIKV antigen 100 DPI. Foci were counted in hippocampal (HC) and cortical regions (N = 15). (B-C) MBP expression was determined by immunofluorescent staining in mid-brain cortex regions of mice (B), expression was normalized to background using the CTCF calculation and is presented as normalized MFI (C; student's t-test; N = 10). (D-F) mPLP expression among mid-brain sections was normalized to background using the CTCF calculation and is presented as normalized MFI in both hippocampus and cortex regions (Two-way ANOVA with Bonferroni's post-hoc analysis; N = 10). (G-I) Vim expression was similarly quantified among hippocampus and cortex regions from infected mice. (Two-way ANOVA with Bonferroni's post-hoc analysis; N = 10). (J) qRT-PCR on pro-inflammatory proteins, pain mediators, MMPs, and anti-inflammatory proteins among infected brains were normalized to GAPDH and then to expression levels of uninfected controls using the $\Delta\Delta Ct$ method (N = 5). For all panels, * is $p < .05$, ** is $p < .01$, *** is $p < .001$, and **** is $p < .0001$. All error bars in all panels reflect standard deviation.

loop.⁶¹ We quantified transcription of *COX2* via qRT-PCR and observed 75-fold greater levels within infected brains. Matrix metalloproteinases (MMPs) are capable of mediating blood-brain barrier (BBB) permeability, and thus we evaluated transcription levels of *MMP2* and *MMP9*. *MMP2* expression increased 466-fold after infection, while *MMP9* increased 290-fold. Finally, we sought to quantify transcription of the anti-inflammatory proteins *IL-10* and *SOCS3*, as

these play prominent roles in controlling neuroinflammation and in regulating anti-inflammatory phenotypes of resident microglia. We observed that these proteins had 15 and 12-fold greater expression after infection. The elevated anti-inflammatory expression is expected at late time points, as these correlate with wound healing. Our transcriptional data suggests that ZIKV infection results in persistent neuroinflammation with high levels of MMPs, which may result

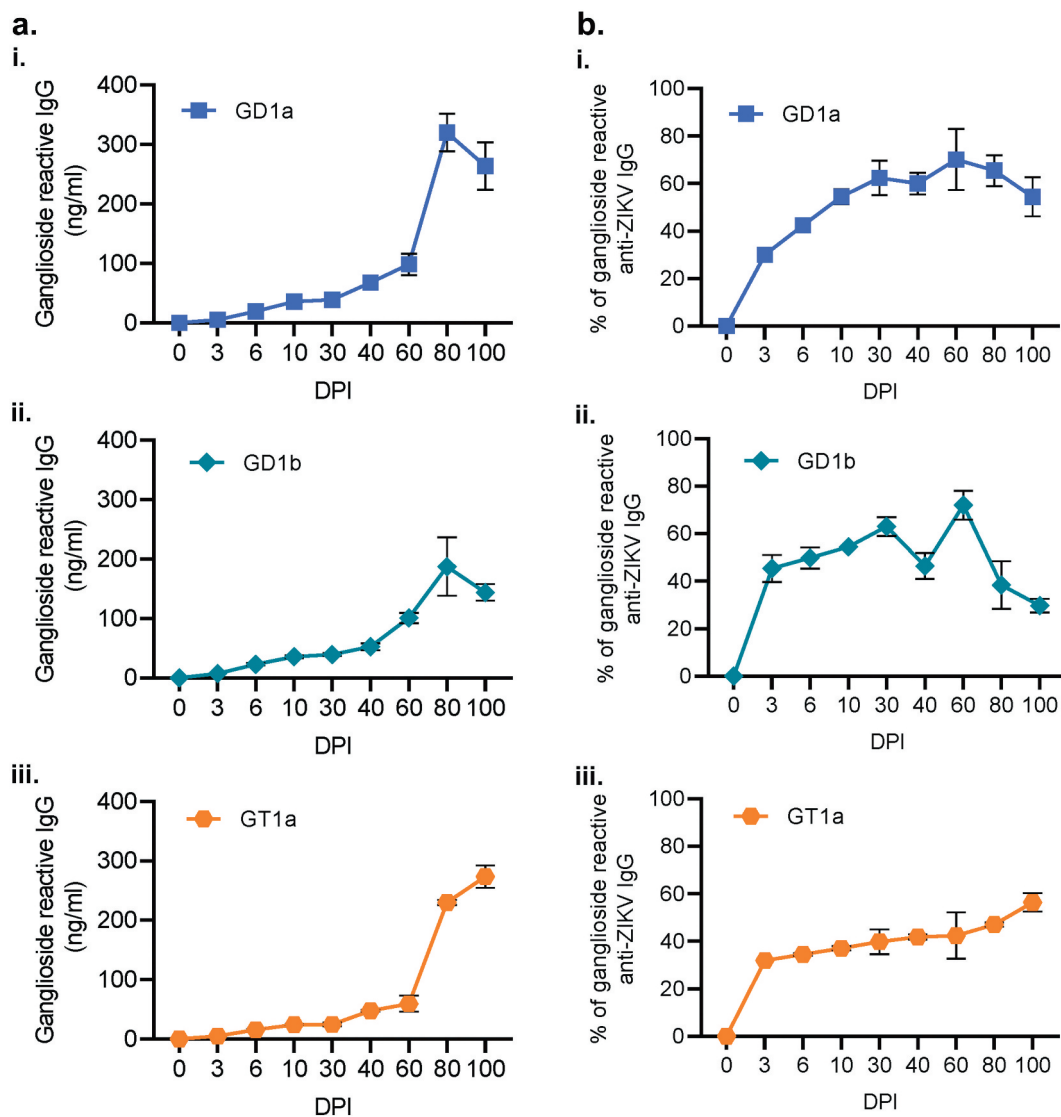


Figure 6. IgG produced during ZIKV infection are cross-reactive to host gangliosides. Antibodies generated during ZIKV infection were also evaluated for their reactivity to GD1a, GD1b, and GT1a gangliosides (Ai, ii, and iii, respectively) via ELISA. The proportion of ganglioside-reactive antibodies to ZIKV-specific IgG was then determined for 0, 3, 10, 60, 80, and 100 DPI. (N = 5). All error bars in all panels reflect standard deviation.

in systemic leukocyte infiltration and contribute to both neurological symptoms and observed demyelination.⁶²

Antibodies generated during ZIKV infection are auto-reactive to GBS-associated neural markers

Current researching regarding GBS and ZIKV-induced GBS points to auto-antibodies generated against glycosylated pathogen proteins that which mimic ganglioside residues on neurons. As our observed neuro-ocular pathology resembles GBS, we next wanted to characterize the ganglioside reactivity of the antibodies generated during ZIKV-infection of immunocompetent mice. Thus, we quantified the total amount of IgG that bound to GD1a, GD1b, and or GT1a gangliosides (Figure 6A i-iii). Each of these gangliosides correlates with a specific variety of GBS. GD1a reactive IgG correlates with acute motor axonal neuropathy; GD1b corresponds to a sensory ataxic variant; GT1a is connected to Miller-Fisher Syndrome, a variant of GBS affecting the eyes.⁶³ To understand what quantity of

these antibodies are auto-reactive, we took the percentage of each ganglioside concentration as a proportion to the total ZIKV-specific IgG (Figure 6B i-iii). As early as 3 DPI, 30–46% of all ZIKV-induced IgG showed reactivity to one of the three gangliosides. Both GD1a and GD1b demonstrated similar peaks at 60 DPI with a maximum of 72% of all ZIKV-IgG being autoreactive. GT1a reached a peak of 56% 100 DPI. Our data demonstrate that highly autoreactive antibodies generated in immunocompetent mice are primarily against GD1a and GD1b gangliosides.

Discussion

In this study, we successfully recapitulated ocular and neurological symptomatology and pathology observed in human ZIKV infections³ and in A129/AG129 murine models using fully immunocompetent BALB/c mice.^{19,56} Importantly, we established precise clinical scoring methods to detail symptom kinetics, severity, and convalescence. We demonstrated that

infection-induced sequelae persist among immune privileged tissues up to 100 DPI, and that the demyelination generated following by ZIKV infection correlates strongly with viral burden and persistence, decreased ocular and motor/neural clinical scores, and non-resolving inflammation. These findings were associated with virus-specific antibodies that, despite being long-lived, were weakly neutralizing and highly enhanced infection, while also perpetuating tissue pathology during ZIKV infection due to autoreactivity. These antibodies were able to neutralize homologous virus but not other ZIKV strains of Asian and African lineages, or DENV serotypes. Notably, they mediated robust infection among non-permissive cells by means of ADE.

Importantly, our study utilized BALB/c mice rather than C57BL/6. Immunocompetent BALB/c mice were preferable for this study because they generate robust humoral responses, and thus are more suitable for investigations about antibody-mediated pathology. While BALB/c have shown retinal degeneration due to normal husbandry lighting, a study by Bell et al. found that standard lighting in animal facilities ranges between 130 and 325 lumens, and induced retinal lesions only in animals ≥ 20 weeks old.⁶⁴ Our results are similar to those reported in C57BL/6 mice that developed retinal and corneal pathology, such as retinal edema and hyperplasia, following ZIKV infection.^{56,65} Manangeeswaran et al. found that retinal lesions and ocular pathology persists in C57BL/6 up to 90 days and correlates with elevated cytokine levels, but was performed in suckling neonatal mice.⁶⁶ Our data in the BALB/c model agree with the findings in C57BL/6 mice, and expand in the field of ZIKV neuro-ocular pathology and the underlying mechanisms, providing further insight into current knowledge gaps.

Our study is the first to report on ZIKV-induced autoreactive antibodies to GD1a, GD1b, and GT1a gangliosides that contribute to myelin degradation in immunocompetent BALB/c mice following infection.⁶⁷ GBS has been correlated with antibody cross-reactivity to host gangliosides in other flaviviruses. We observed that 25–75% of all antibodies generated by and specific to PRVABC59 were also reactive to GD1a and GD1b gangliosides, which may correlate to our observed motor-neural pathology.⁶⁸ Gangliosides are vital to synaptic transmissions, intercellular adhesion and communication, equilibrium, immune signaling, and nervous system and motor/neural network maintenance.⁶⁹ Anti-ganglioside antibodies have been previously shown to lead to the absence or fragmentation of MBP, myelin PLP, and vimentin all contributing to persistent neuroinflammation within the brain by acting as damage associated molecular patterns (DAMPs). Myelin or myelin debris signal in macrophages via complement/opsonization or phagocytosis and facilitate M1 (macrophage type-1) polarization and proinflammatory secretion.⁷⁰ Protracted neuroinflammation by M1 microglia is mediated by locally secreted inflammatory factors, such as TNF- α , which is consistent with our transcriptional data.⁷⁰

The persistent neuroinflammation and severe pathology we observed is consistent with published data reporting that chronic neuroinflammation potentiates severe motor/cognitive diseases among flavivirus infections as seen in GBS cases.⁷¹ COX2 stimulates glial cell IL-1 β and TNF- α secretion resulting in a paracrine and autocrine signaling cascade.⁷² This cycle of

persistent inflammation and pain-sensitivity is established through a COX2 and IL-1 β positive feedback loop, via NF- κ B signaling.^{61,73} Our data confirmed this in ZIKV-infected mice, showing elevated transcription of COX2, IL-1 β , and TNF- α up to 100 days after infection while simultaneously exhibiting persistently hypo- and areflexia.

MMPs are endopeptidases with vital functions such as neural network remodeling, tissue formation, and BBB integrity regulation. M2 microglia (type 2 macrophages), which function in tissue remodeling and anti-inflammatory responses, secrete MMP2 to permeabilize the BBB⁷⁰ and allow for infiltrating macrophages to enter the brain, phagocytose, and clear dead cells.^{62,74} Increased permeability of the BBB via elevated transcription of MMP2 and MMP9 corresponds with increased inflammatory leukocyte trafficking into the brain.^{75,76} Our findings on MMP2 and MMP9 elevation following ZIKV infection are similar to those of Wang et al., where MMP2 and MMP9 were upregulated in brain tissues following West Nile virus (WNV) infection, thus mediating infiltrating leukocyte trafficking into the brain.⁷²

TNF- α and IL-6 production by local resident and infiltrating immune cells in the CNS induces IL-10 production, which has an anti-inflammatory function via SOCS3 signaling pathways.⁷⁷ Importantly, IL-10 has demonstrated the ability to protect astrocytes from excessive inflammation and in regulating adult neurogenesis after brain injury, being implicated as an important mediator of intracellular cross talk between microglia, astrocytes, neurons, and oligodendrocytes.^{78,79}

In eyes, COX2, IL-1 β , TNF- α , MMP2, and MMP9 transcription profiles among infected animals were elevated through 100 DPI. Interestingly, IL-10 and SOCS3 expression were also elevated in this cohort, suggesting an alternative route of ocular pathogenesis in addition to the primary route resulting from infection and inflammation. High intraocular concentrations of IL-10 and SOCS3 have resulted in pathological angiogenesis via Müller-cell mediated neovascularization.⁸⁰ Additionally, SOCS3 works by blocking intracellular signaling of IL-6 and IL-23, namely preventing STAT3 phosphorylation and directly influencing ocular T cell repertoires.⁸¹ This constraint on T_{H1} and T_{H17} differentiation during infection and inflammation also provides insight into a novel pathway for ZIKV pathogenesis in the eye.

Our study addresses a current gap in the field regarding antibody-specific mechanisms that underlie the initiation of ocular and neurological pathology persistence and damage, and point to the need for a more comprehensive, systems biology approach to understand how antibodies influence long-term neurological pathogenesis of flaviviruses. Collectively, our data suggests that autoreactivity of ZIKV antibodies may initiate a demyelination cascade that ultimately results in chronic neuroinflammation and persistent neuro-ocular impairments. Importantly, we demonstrate immunocompetent animals can serve as models for pathogenesis and long-term infection studies. These findings underscore the need of exploring alternative vaccination platforms and imposing stringent qualifications for ZIKV vaccine candidates that would confer breadth and longevity of protection while minimizing the risk of autoimmunity or ADE. Future studies should include investigation of

demyelination sequelae after passive transfer of ZIKV-induced antibodies, and the putative role of maternal antibodies on vertically transmission. Additionally, future studies duplicating this work in C57BL/6 mice will determine if similar pathology can be observed in a Th1-skewed background.

Acknowledgments

We thank Dr. Sharon Isern, Dr. Scott Michael, and Lauren Paul for providing the ZIKV PRVABC59 strain for propagation.

We thank Dr. Micah Chrenek, Dr. Hans Grossniklaus, and Dr. John Nickerson from Emory Ophthalmology Clinic for their advice on optic histology and staining.

We thank Dr. Eugenia Skountzou and Dr. Nikolaos Papaioannou for their expertise in veterinary ophthalmology and for detailed assistance in evaluating animal ocular pathology.

We thank Vidisha Singh and Aaron Scanlon for assistance running qRT-PCR experiments.

Funding

This work was supported by NIAID and CEIRS – HHSN272201400004C NIAID National Institute of Allergy and Infectious Diseases [HHSN272201400004C NIAID];

ORCID

Ioanna Skountzou  <http://orcid.org/0000-0002-6429-244X>

Author contribution

J.T.B., N.L., I.S., E.S. Project conceptualization and experimental design
J.T.B., L.K.M., E.S.E., D.S., N.L., O.Q.A., E.Q.L., I.S.: Execution of experiments

E.S. and N.P. Assessment of ocular pathology

J.T.B., N.L., D.S., and I.S. Data analysis.

J.T.B., D.S. and I.S. Manuscript preparation

R.W.C. Manuscript feedback.

All authors read and provided feedback prior to submission

Competing financial interests

J.T.B., L.K.M., E.S.E., D.S., N.L., O.Q.A., E.S., N.P., D.T.W., and I.S. declare that they have no conflicts of interest.

Ethics statement

Emory University Division of Animal Resources veterinary staff ascertained welfare of animals in addition to research scientists. DAR staff also performed regular care and wellness assessments. Animal work was conducted according to Emory University Institutional Animal Care and Use Committee (IACUC) guidelines according to an approved protocol (DAR2002950-122617BN) in accordance with the United States federal Animal Welfare Act (PL 89-544) and subsequent amendments. Emory University is registered with the United States Department of Agriculture (57-R-003) and has filed an Assurance of Compliance statement with the Office of Laboratory Animal Welfare of the National Institutes of Health (D16-00113). Emory University has been fully and continuously accredited by AAALAC International since 1992 (Unit 000781). The Georgia Fee-Exempt Wild Animal Permit Customer Number for animals maintained by the Division of Animal Resources is 22257.

References

1. Beaver JT, Lelutiu N, Habib R, Skountzou I. Evolution of two major zika virus lineages: implications for pathology, immune response, and vaccine development. *Front Immunol.* 2018;9(1640). doi:10.3389/fimmu.2018.01640.
2. Araujo LM, Ferreira ML, Nascimento OJ. Guillain-Barre syndrome associated with the Zika virus outbreak in Brazil. *Arq Neuropsiquiatr.* 2016;74(253–255). doi:10.1590/0004-282X20160035.
3. Brasil P, Pereira JP, Moreira ME, Ribeiro Nogueira RM, Halai U-A, Salles TS, *et al.* Zika virus infection in pregnant Women in Rio de Janeiro. *N Engl J Med.* 2016;375(2321–2334). doi:10.1056/NEJMoa1602412
4. da Silva IRF, Frontera JA, Bispo de Filippis AM, Nascimento O, Group R-G-ZR. Neurologic complications associated with the Zika Virus in Brazilian adults. *JAMA Neurol.* 2017;74(1190–1198). doi:10.1001/jamaneurol.2017.1703.
5. Bandyopadhyay D, Hajra A. ZIKA virus: A new threat to the eyes. *Eur J Intern Med.* 2017;44:e9–e10. doi:10.1016/j.ejim.2017.05.022.
6. Prakalapakorn SG, Meaney-Delman D, Honein MA, Rasmussen SA. The eyes as a window to improved understanding of the prenatal effects of Zika virus infection. *J Aapos.* 2017;21(259–261). doi:10.1016/j.jaapos.2017.07.001.
7. Ramakrishnan S, Kannan B, Kannan A, Venkatesan EP. Vision loss in guillain-barre syndrome: is it a complication of guillain-barre syndrome or just a coincidence? *J Ophthalmic Vis Res.* 2016;11:340–41. doi:10.4103/2008-322X.188405.
8. Barzon L, Pacenti M, Franchin E, Lavezzo E, Trevisan M, Sgarabotto D, Palu G. Infection dynamics in a traveller with persistent shedding of Zika virus RNA in semen for six months after returning from Haiti to Italy, January 2016. *Euro Surveill.* 2016;21. doi:10.2807/1560-7917.ES.2016.21.32.30316.
9. Mansuy JM, Dutertre M, Mengelle C, Fourcade C, Marchou B, Delobel P, Izopet J, Martin-Blondel G. Zika virus: high infectious viral load in semen, a new sexually transmitted pathogen? *Lancet Infect Dis.* 2016;16:405. doi:10.1016/S1473-3099(16)00138-9.
10. Murray KO, Gorchakov R, Carlson AR, Berry R, Lai L, Natrajan M, Garcia MN, Correa A, Patel SM, Aagaard K, Mulligan MJ. Prolonged detection of zika virus in vaginal secretions and whole blood. *Emerg Infect Dis.* 2017;23(99–101). doi:10.3201/eid2301.161394
11. Bautista LE. Zika virus infection and risk of Guillain-Barre syndrome: A meta-analysis. *J Neurol Sci.* 2019;403(99–105). doi:10.1016/j.jns.2019.06.019.
12. Munoz LS, Parra B, Pardo CA, Neuroviruses Emerging in the Americas, S. Neurological Implications of Zika Virus Infection in Adults. *J Infect Dis.* 2017;216:S897–S905. doi:10.1093/infdis/jix511.
13. Barbi L, Coelho AVC, Alencar LCA, Crovella S. Prevalence of Guillain-Barre syndrome among Zika virus infected cases: a systematic review and meta-analysis. *Braz J Infect Dis.* 2018;22(137–141). doi:10.1016/j.bjid.2018.02.005.
14. Dimachkie MM, Barohn RJ. Guillain-Barre syndrome and variants. *Neurol Clin.* 2013;31(491–510). doi:10.1016/j.ncl.2013.01.005.
15. Nachamkin I, Allos BM, Ho T. Campylobacter species and Guillain-Barre syndrome. *Clin Microbiol Rev.* 1998;11:555–67. doi:10.1128/CMR.11.3.555.
16. Garber C, Soung A, Vollmer LL, Kanmogne M, Last A, Brown J, Klein RS. T cells promote microglia-mediated synaptic elimination and cognitive dysfunction during recovery from neuropathogenic flaviviruses. *Nat Neurosci.* 2019;22(1276–1288). doi:10.1038/s41593-019-0427-y.
17. McDonald EM, Duggal NK, Delorey MJ, Oksanish J, Ritter JM, Brault AC. Duration of seminal Zika viral RNA shedding in immunocompetent mice inoculated with Asian and African genotype viruses. *Virology.* 2019;535(1–10). doi:10.1016/j.virol.2019.06.010.
18. Munoz-Jordan JL, Fredericksen BL. How flaviviruses activate and suppress the interferon response. *Viruses.* 2010;2(676–691). doi:10.3390/v2020676.

19. Dowall SD, Graham VA, Rayner E, Atkinson B, Hall G, Watson RJ, Bosworth A, Bonney LC, Kitchen S, Hewson R, et al. A susceptible mouse model for zika virus infection. *PLoS Negl Trop Dis*. 2016;10(e0004658). doi:10.1371/journal.pntd.0004658
20. Lazear HM, Govero J, Smith A, Platt D, Fernandez E, Miner J, Diamond M. A mouse model of zika virus pathogenesis. *Cell Host Microbe*. 2016;19(720–730). doi:10.1016/j.chom.2016.03.010
21. Zhao Z, Yang M, Azar SR, Soong L, Weaver SC, Sun J, Chen Y, Rossi SL, Cai J. Viral retinopathy in experimental models of Zika infection. *Invest Ophthalmol Vis Sci*. 2017;58(4355–4365). doi:10.1167/iovs.17-22016
22. Singh PK, Guest J-M, Kanwar M, Boss J, Gao N, Juzych MS, Abrams GW, Yu F-S, Kumar A. Zika virus infects cells lining the blood-retinal barrier and causes chorioretinal atrophy in mouse eyes. *JCI Insight*. 2017;2(e92340). doi:10.1172/jci.insight.92340
23. Simonin Y, Erkilic N, Damodar K, Clé M, Desmetz C, Bolloré K, Taleb M, Torriano S, Barthelemy J, Dubois G, et al. Zika virus induces strong inflammatory responses and impairs homeostasis and function of the human retinal pigment epithelium. *EBioMedicine*. 2019;39(315–331). doi:10.1016/j.ebiom.2018.12.010
24. Morrison TE, Diamond MS. Animal models of zika virus infection, pathogenesis, and immunity. *J Virol*. 2017;91. doi:10.1128/JVI.00009-17
25. Nazerai L, Schøller AS, Rasmussen POS, Buus S, Stryhn A, Christensen JP, Thomsen AR. A New In Vivo Model to Study Protective Immunity to Zika Virus Infection in Mice With Intact Type I Interferon Signaling. *Front Immunol*. 2018;9(593). doi:10.3389/fimmu.2018.00593
26. Coelho SVA, Neris RLS, Papa MP, Schnellrath LC, Meuren LM, Tschöcke DA, Leomil L, Verçoza BRF, Miranda M, Thompson FL, et al. Development of standard methods for Zika virus propagation, titration, and purification. *J Virol Methods*. 2017;246(65–74). doi:10.1016/j.jviromet.2017.04.011
27. Matrosovich M, Matrosovich T, Garten W, Klenk HD. New low-viscosity overlay medium for viral plaque assays. *Virology*. 2006;3(63). doi:10.1186/1743-422X-3-63
28. Priyamvada L, Quicke KM, Hudson WH, Onlamoon N, Sewatanon J, Edupuganti S, Pattanapanyasat K, Chokephaibulkit K, Mulligan MJ, Wilson PC, et al. Human antibody responses after dengue virus infection are highly cross-reactive to Zika virus. *Proc Natl Acad Sci U S A*. 2016;113(7852–7857). doi:10.1073/pnas.1607931113
29. Garcia-Nicolas O, Braun RO, Milona P, Lewandowska M, Dijkman R, Alves MP, Summerfield A. Targeting of the Nasal Mucosa by Japanese Encephalitis Virus for Non-Vector-Borne Transmission. *J Virol*. 2018;92. doi:10.1128/JVI.01091-18
30. Hassert M, Wolf KJ, Schwetye KE, DiPaolo RJ, Brien JD, Pinto AK. CD4+T cells mediate protection against Zika associated severe disease in a mouse model of infection. *PLoS Pathog*. 2018;14(e1007237). doi:10.1371/journal.ppat.1007237
31. Flammer J, Konieczka K, Bruno RM, Virdis A, Flammer AJ, Taddei S. The eye and the heart. *Eur Heart J*. 2013;34(1270–1278). doi:10.1093/eurheartj/eh023
32. Gzabert K, McColl BW. Isolation and Phenotyping of Adult Mouse Microglial Cells. *Methods Mol Biol*. 2018;1784(77–86). doi:10.1007/978-1-4939-7837-3_7
33. Lee JK, Tansey MG. Microglia isolation from adult mouse brain. *Methods Mol Biol*. 2013;1041(17–23). doi:10.1007/978-1-62703-520-0_3
34. Sapparapu G, Fernandez E, Kose N, Cao B, Fox JM, Bombardi RG, Zhao H, Nelson CA, Bryan AL, Barnes T, et al. Neutralizing human antibodies prevent Zika virus replication and fetal disease in mice. *Nature*. 2016;540(443–447). doi:10.1038/nature20564
35. Mavigner M, Raper J, Kovacs-Balint Z, Gumber S, O'Neal JT, Bhaumik SK, Zhang X, Habib J, Mattingly C, McDonald CE, et al. Postnatal Zika virus infection is associated with persistent abnormalities in brain structure, function, and behavior in infant macaques. *Sci Transl Med*. 2018;10. doi:10.1126/scitranslmed.aao6975
36. Taib T, Leconte C, Van Steenwinckel J, Cho AH, Palmier B, Torsello E, Lai Kuen R, Onyeomah S, Ecomard K, Benedetto C, et al. Neuroinflammation, myelin and behavior: temporal patterns following mild traumatic brain injury in mice. *PLoS One*. 2017;12(e0184811). doi:10.1371/journal.pone.0184811
37. Brayton C, McBean NF, Watson J. JHU Mouse Pathobiology & Phenotyping Short Course. *Johns Hopkins Univ Sch Med Dep Mol Comp Pathol*. 2015;4(1–10).
38. Drapeau E, Riad M, Kajiwarra Y, Buxbaum JD. Behavioral Phenotyping of an Improved Mouse Model of Phelan-McDermid Syndrome with a Complete Deletion of the Shank3 Gene. *eNeuro*. 2018;5. doi:10.1523/ENEURO.0046-18.2018
39. Olsen CM, Childs DS, Stanwood GD, Winder DG. Operant sensation seeking requires metabotropic glutamate receptor 5 (mGluR5). *PLoS One*. 2010;5(e15085). doi:10.1371/journal.pone.0015085
40. Ferrari G, Chauhan SK, Ueno H, Nallasamy N, Gandolfi S, Borges L, Dana R. A novel mouse model for neurotrophic keratopathy: trigeminal nerve stereotactic electrolysis through the brain. *Invest Ophthalmol Vis Sci*. 2011;52(2532–2539). doi:10.1167/iovs.10-5688
41. Ronca SE, Smith J, Koma T, Miller MM, Yun N, Dineley KT, Paessler S. Mouse Model of Neurological Complications Resulting from Encephalitic Alphavirus Infection. *Front Microbiol*. 2017;8(188). doi:10.3389/fmicb.2017.00188
42. Blivis D, Haspel G, Mannes PZ, O'Donovan MJ, Iadarola MJ. Identification of a novel spinal nociceptive-motor gate control for Adelta pain stimuli in rats. *Elife*. 2017;6. doi:10.7554/eLife.23584
43. Plotnikov MB, Chernysheva GA, Aliev OI, Smol'iakova VI, Fomina TI, Osipenko AN, Rydchenko VS, Anfinogenova YJ, Khlebnikov AI, Schepetkin IA, et al. Protective effects of a new C-Jun N-terminal Kinase inhibitor in the model of global cerebral ischemia in rats. *Molecules*. 2019;24. doi:10.3390/molecules24091722
44. Neugebauer V, Han JS, Adwanikar H, Fu Y, Ji G. Techniques for assessing knee joint pain in arthritis. *Mol Pain*. 2007;3(8). doi:10.1186/1744-8069-3-8
45. O'Leary TP, Robertson A, Chipman PH, Rafuse VF, Brown RE. Motor function deficits in the 12 month-old female 5xFAD mouse model of Alzheimer's disease. *Behav Brain Res*. 2018;337(256–263). doi:10.1016/j.bbr.2017.09.009
46. Fink SL, Cookson BT. Apoptosis, pyroptosis, and necrosis: mechanistic description of dead and dying eukaryotic cells. *Infect Immun*. 2005;73(1907–1916). doi:10.1128/IAI.73.4.1907-1916.2005
47. Miao EA, Rajan JV, Aderem A. Caspase-1-induced pyroptotic cell death. *Immunol Rev*. 2011;243(206–214). doi:10.1111/j.1600-065X.2011.01044.x
48. Yang M, Antoine DJ, Weemhoff JL, Jenkins RE, Farhood A, Park BK, Jaeschke H. Biomarkers distinguish apoptotic and necrotic cell death during hepatic ischemia/reperfusion injury in mice. *Liver Transpl*. 2014;20(1372–1382). doi:10.1002/lt.23958
49. Lourenco T, Paes de Faria J, Bippes CA, Maia J, Lopes-da-Silva JA, Relvas JB, Grãos M. Modulation of oligodendrocyte differentiation and maturation by combined biochemical and mechanical cues. *Sci Rep*. 2016;6(21563). doi:10.1038/srep21563
50. Esser ES, Romanyuk A, Vassilieva EV, Jacob J, Prausnitz MR, Compans RW, Skountzou I. Tetanus vaccination with a dissolving microneedle patch confers protective immune responses in pregnancy. *J Control Release*. 2016;236(47–56). doi:10.1016/j.jconrel.2016.06.026
51. Oduybo T, Polen KD, Walke H, Reagan-steiner S, Lathrop E, Rabe IB, Kuhnert-Tallman WL, Martin SW, Walker AT, Gregory CJ, et al. Update: interim guidance for health care providers caring for pregnant women with possible Zika Virus Exposure — United States(Including U.S. Territories), July 2017. *Morbidity and Mortality Weekly Report*. *Surveil Summ*. 2017;66:781–93.
52. Cao-Lormeau VM, Blake A, Mons S, Lastère S, Roche C, Vanhomwegen J, Dub T, Baudouin L, Teissier A, Larre P, et al. Guillain-Barre Syndrome outbreak associated with Zika virus infection in French Polynesia: a case-control study. *Lancet*. 2016;387(1531–1539). doi:10.1016/S0140-6736(16)00562-6

53. Yun H, Rowe AM, Lathrop KL, Harvey SA, Hendricks RL. Reversible nerve damage and corneal pathology in murine herpes simplex stromal keratitis. *J Virol.* 2014;88(7870–7880). doi:10.1128/JVI.01146-14.
54. Chucair-Elliott AJ, Zheng M, Carr DJ. Degeneration and regeneration of corneal nerves in response to HSV-1 infection. *Invest Ophthalmol Vis Sci.* 2015;56(1097–1107). doi:10.1167/iovs.14-15596.
55. Martin-Acebes MA, Saiz JC, Jimenez de Oya N. Antibody-Dependent Enhancement and Zika: real Threat or Phantom Menace? *Front Cell Infect Microbiol.* 2018;8:44. doi:10.3389/fcimb.2018.00044.
56. Miner JJ, Sene A, Richner JM, Smith AM, Santeford A, Ban N, Weger-Lucarelli J, Manzella F, Rückert C, Govero J, et al. Zika virus infection in mice causes panuveitis with shedding of virus in tears. *Cell Rep.* 2016;16(3208–3218). doi:10.1016/j.celrep.2016.08.079
57. Langford DJ, Bailey AL, Chanda ML, Clarke SE, Drummond TE, Echols S, Glick S, Ingrao J, Klassen-Ross T, LaCroix-Fralish ML, et al. Coding of facial expressions of pain in the laboratory mouse. *Nat Methods.* 2010;7(447–449). doi:10.1038/nmeth.1455
58. Matsumiya LC, Sorge RE, Sotocinal SG, Tabaka JM, Wieskopf JS, Zaloum A, King OD, Mogil JS. Using the Mouse Grimace Scale to reevaluate the efficacy of postoperative analgesics in laboratory mice. *J Am Assoc Lab Anim Sci.* 2012;51:42–49.
59. Ubogu EE. Inflammatory neuropathies: pathology, molecular markers and targets for specific therapeutic intervention. *Acta Neuropathol.* 2015;130(445–468). doi:10.1007/s00401-015-1466-4.
60. Fulton D, Paez PM, Campagnoni AT. The multiple roles of myelin protein genes during the development of the oligodendrocyte. *ASN Neuro.* 2010;2(e00027). doi:10.1042/AN20090051.
61. Samad TA, Moore KA, Sapirstein A, Billet S, Allchorne A, Poole S, Bonventre JV, Woolf CJ. Interleukin-1beta-mediated induction of Cox-2 in the CNS contributes to inflammatory pain hypersensitivity. *Nature.* 2001;410(471–475). doi:10.1038/35068566.
62. Konnecke H, Bechmann I. The role of microglia and matrix metalloproteinases involvement in neuroinflammation and gliomas. *Clin Dev Immunol.* 2013;2013(914104). doi:10.1155/2013/914104.
63. Naik GS, Meena AK, Reddy BAK, Mridula RK, Jabeen SA, Borgohain R. Anti-ganglioside antibodies profile in Guillain-Barre syndrome: correlation with clinical features, electrophysiological pattern, and outcome. *Neurol India.* 2017;65(1001–1005). doi:10.4103/neuroindia.NI_1226_15
64. Bell BA, Kaul C, Bonilha VL, Rayborn ME, Shadrach K, Hollyfield JG. The BALB/c mouse: effect of standard vivarium lighting on retinal pathology during aging. *Exp Eye Res.* 2015;135(192–205). doi:10.1016/j.exer.2015.04.009.
65. Singh PK, Kasetti RB, Zode GS, Goyal A, Juzych MS, Kumar A. Zika Virus Infects Trabecular Meshwork and Causes Trabeculitis and Glaucomatous Pathology in Mouse Eyes. *mSphere.* 2019;4. doi:10.1128/mSphere.00173-19.
66. Manangeswaran M, Kielczewski JL, Sen HN, Xu BC, Ireland DDC, McWilliams IL, Chan -C-C, Caspi RR, Verthelyi D. ZIKA virus infection causes persistent chorioretinal lesions. *Emerg Microb Infect.* 2018;7(96). doi:10.1038/s41426-018-0096-z.
67. Ponomarenko NA, Durova OM, Vorobiev II, Belogurov AA, Kurkova IN, Petrenko AG, Telegin GB, Suchkov SV, Kiselev SL, Lagarkova MA, et al. Autoantibodies to myelin basic protein catalyze site-specific degradation of their antigen. *Proc Natl Acad Sci U S A.* 2006;103(281–286). doi:10.1073/pnas.0509849103
68. Paul LM, Carlin ER, Jenkins MM, Tan AL, Barcellona CM, Nicholson CO, Michael SF, Isern S. Dengue virus antibodies enhance Zika virus infection. *Clin Transl Immunol.* 2016;5(e117). doi:10.1038/cti.2016.72
69. Komagamine T, Matsuno K, Sakumoto Y, Takahashi H, Kokubun N, Yuki N, Hirata K. Immunohistochemical localization of the GM1, GD1a, GD1b and GQ1b gangliosides in the neuronal endings of rat muscle spindles. *Arch Histol Cytol.* 2013;74:31–40. doi:10.1679/aohc.74.31.
70. Kopper TJ, Gensel JC. Myelin as an inflammatory mediator: myelin interactions with complement, macrophages, and microglia in spinal cord injury. *J Neurosci Res.* 2018;96:969–77. doi:10.1002/jnr.24114.
71. Frankola KA, Greig NH, Luo W, Tweedie D. Targeting TNF-alpha to elucidate and ameliorate neuroinflammation in neurodegenerative diseases. *CNS Neurol Disord Drug Targets.* 2011;10:391–403. doi:10.2174/187152711794653751.
72. Wang P, Dai J, Bai F, Kong KF, Wong SJ, Montgomery RR, Madri JA, Fikrig E. Matrix metalloproteinase 9 facilitates West Nile virus entry into the brain. *J Virol.* 2008;82:8978–85. doi:10.1128/JVI.00314-08.
73. Mori T, Miyamoto T, Yoshida H, Asakawa M, Kawasumi M, Kobayashi T, Morioka H, Chiba K, Toyama Y, Yoshimura A, et al. IL-1beta and TNFalpha-initiated IL-6-STAT3 pathway is critical in mediating inflammatory cytokines and RANKL expression in inflammatory arthritis. *Int Immunol.* 2011;23(701–712). doi:10.1093/intimm/dxr077
74. Ashley SL, Pretto CD, Stier MT, Kadiyala P, Castro-Jorge L, Hsu T-H, Doherty R, Carnahan KE, Castro MG, Lowenstein PR, et al. Matrix Metalloproteinase Activity in Infections by an Encephalitic Virus, Mouse Adenovirus Type 1. *J Virol.* 2017;91. doi:10.1128/JVI.01412-16.
75. Rempe RG, Hartz AMS, Bauer B. Matrix metalloproteinases in the brain and blood-brain barrier: versatile breakers and makers. *J Cereb Blood Flow Metab.* 2016;36(1481–1507). doi:10.1177/0271678X16655551.
76. Song J, Wu C, Korpos E, Zhang X, Agrawal SM, Wang Y, Faber C, Schafers M, Korner H, Opendakker G, et al. Focal MMP-2 and MMP-9 activity at the blood-brain barrier promotes chemokine-induced leukocyte migration. *Cell Rep.* 2015;10(1040–1054). doi:10.1016/j.celrep.2015.01.037
77. DiSabato DJ, Quan N, Godbout JP. Neuroinflammation: the devil is in the details. *J Neurochem.* 2016;139(Suppl 2):136–53. doi:10.1111/jnc.13607.
78. Burmeister AR, Marriotti I. The Interleukin-10 Family of Cytokines and Their Role in the CNS. *Front Cell Neurosci.* 2018;12(458). doi:10.3389/fncel.2018.00458.
79. Khaiboullina S, Uppal T, Kletenkov K, St. Jeor SC, Garanina E, Rizvanov A, Verma SC. Transcriptome Profiling Reveals Pro-Inflammatory Cytokines and Matrix Metalloproteinase Activation in Zika Virus Infected Human Umbilical Vein Endothelial Cells. *Front Pharmacol.* 2019;10(642). doi:10.3389/fphar.2019.00642.
80. Nakamura R, Sene A, Santeford A, Gdoura A, Kubota S, Zapata N, Apte RS. IL10-driven STAT3 signalling in senescent macrophages promotes pathological eye angiogenesis. *Nat Commun.* 2015;6(7847). doi:10.1038/ncomms8847.
81. Baker BJ, Akhtar LN, Benveniste EN. SOCS1 and SOCS3 in the control of CNS immunity. *Trends Immunol.* 2009;30(392–400). doi:10.1016/j.it.2009.07.001.